INTERNATIONAL JOURNAL FOR NUMERICAL METHODS IN BIOMEDICAL ENGINEERING
Int. J. Numer. Meth. Biomed. Engng. (2011)
Published online in Wiley Online Library (wileyonlinelibrary.com). DOI: 10.1002/cnm.1452

Partial differential equation transform—Variational formulation and Fourier analysis

Yang Wang [1], Guo-Wei Wei [1,2,*,†] and Siyang Yang [1]

[1] *Department of Mathematics, Michigan State University, MI 48824, U.S.A.*
[2] *Department of Electrical and Computer Engineering, Michigan State University, MI 48824, U.S.A.*

SUMMARY

Nonlinear partial differential equation (PDE) models are established approaches for image/signal processing, data analysis, and surface construction. Most previous geometric PDEs are utilized as low-pass filters, which give rise to image trend information. In an earlier work, we introduced mode decomposition evolution equations (MoDEEs), which behave like high-pass filters and are able to systematically provide intrinsic mode functions (IMFs) of signals and images. Because of their tunable time–frequency localization and perfect reconstruction, the operation of MoDEEs is called a PDE transform. By appropriate selection of PDE transform parameters, we can tune IMFs into trends, edges, textures, noise, and so forth, which can be further utilized in the secondary processing for various purposes. This work introduces variational formulation, performs the Fourier analysis, and conducts biomedical and biological applications of the proposed PDE transform. The variational formulation offers an algorithm to incorporate two image functions and two sets of low-pass PDE operators in the total energy functional. Two low-pass PDE operators have different signs, leading to energy disparity, while a coupling term, acting as a relative fidelity of two image functions, is introduced to reduce the disparity of two energy components. We construct variational PDE transforms by using Euler–Lagrange equation and artificial time propagation. Fourier analysis of a simplified PDE transform is presented to shed light on the filter properties of high-order PDE transforms. Such an analysis also offers insight on the parameter selection of the PDE transform. The proposed PDE transform algorithm is validated by numerous benchmark tests. In one selected challenging example, we illustrate the ability of PDE transform to separate two adjacent frequencies of $\sin(x)$ and $\sin(1.1x)$. Such an ability is due to PDE transform's controllable frequency localization obtained by adjusting the order of PDEs. The frequency selection is achieved either by diffusion coefficients or by propagation time. Finally, we explore a large number of practical applications to further demonstrate the utility of the proposed PDE transform. Copyright © 2011 John Wiley & Sons, Ltd.

Received 12 March 2011; Revised 20 April 2011; Accepted 27 April 2011

KEY WORDS: mode decomposition; evolution equations; anisotropic diffusion; total variation; high-pass filter; partial differential equation transform

1. INTRODUCTION

Processing and analysis of signal, sound, data, image, surface, or video frame have been an important issue in a general category of subjects, including computer vision, face recognition, feature detection, medical diagnosis, remote sensing, machine vision, and artificial intelligence [1–4]. Signal, image, surface, and data processing are realized via a family of operations and algorithms, such as filtering, smoothing, denoising (or deblurring), enhancement, segmentation, reconstruction, pattern recognition, surface analysis, and construction. The advance in signal, image, surface, and data analysis also benefits many related fields, such as optical sorting, automatic control, augmented reality, robotics, sonar, radar, communication, navigation, biomolecular modeling, and a variety of

*Correspondence to: Guo-Wei Wei, Department of Mathematics, Michigan State University, Lansing, MI 48824, U.S.A.
†E-mail: wei@math.msu.edu

Copyright © 2011 John Wiley & Sons, Ltd.

imaging modalities. There are a variety of algorithms for signal, image, surface, and data processing. The essential idea is the use of filters, such as linear, nonlinear, active, passive, low-pass, high-pass, Fourier, wavelet, Chebyshev, Gaussian, Kalman, Wiener, and conjugate filters [5–8]. Decomposition of the original signal, image, surface, and data into various modes according to their mathematical features and frequency distributions is a key procedure in all the aforementioned applications. Usually, the subsequent analysis, also called secondary processing, on individual mode components enables us to achieve our goal of signal, image, surface, and data analysis. Therefore, mode decomposition is a fundamental process in information processing and data analysis.

Fourier or spectral analysis is a classical technique for mode decomposition and remains to be a powerful tool in signal, image, and data processing [1, 4, 9–11]. However, Fourier analysis is not suitable for studying data of non-stationary nature, and it may be difficult to choose a suitable window size to satisfy the conflicting requirements of localizing an event in time and resolving its frequency distribution. Moreover, the method is not data adaptive. In many signal-processing applications, one usually desires the information of detailed position and momentum relation, which is also lacking in Fourier spectral analysis. Furthermore, Fourier analysis is less ideal for applications in image processing when localized visual features like edges need to be detected. Most importantly, when the signal or image involves abundantly many modes, the subsequent analysis or secondary processing becomes awkward if it is not fully automatic.

Wavelet transform is another popular technique for mode decomposition and shows a great power in analyzing unsteady and non-stationary data [1, 2, 4, 12–17]. The fundamental idea behind wavelet filters is to analyze data according to their scales. In this sense, wavelets realize the locality by resorting to localized multiscale bases, which are usually more appropriate than sines and cosines in the Fourier basis, and by decomposing signals into various sub-bands. Because individual wavelet functions can be localized in space, whereas Fourier sine and cosine functions are not, many functions become 'sparse' in wavelet bases. By dilation and translation, wavelet transform usually yields much fewer number of non-trivial sub-bands than the number of Fourier modes, and thus results in many useful applications such as data compression, detecting features in images, and removing noise from time series. Wavelet methods thus provide an efficient approach for image mode decomposition and secondary processing. Most modes separated by wavelet transform are usually closely related to the edge information or global feature of the whole image. Therefore, wavelets are efficient for image compression. Overall, the wavelet methods are more adaptive than Fourier analysis. However, wavelet analysis is basically a linear analysis and suffers from many limitations. The down sides include uniformly poor resolution, sometimes counter-intuitive interpretation, and non-data adaptive nature as the same wavelet basis is used to analyze all the data [18]. Moreover, wavelet methods inherit many drawbacks of the Fourier analysis because many commonly used wavelets were originated from Fourier analysis.

Witkin [19] introduced the diffusion equation for image denoising in 1983. The central idea is that the evolution of an image under a diffusion operator is formally equivalent to the standard Gaussian low-pass filter, which is commonly used for image denoising. In 1990, Perona and Malik [20] proposed an anisotropic diffusion equation, which is able to remove noise without smearing the image edges too much. In the anisotropic diffusion equation, the diffusion coefficient is replaced by a function of image gradients such that the diffusion coefficient is small at the image edges [20–24]. Therefore, the Perona–Malik equation is nonlinear. Despite of better image edge protection, the nonlinear anisotropic diffusion operator may break down when the gradient generated by noise is comparable with the image edges and features [25, 26]. Application of a pre-convolution with a smoothing function to the image can practically alleviate the instability and reduce gray scale oscillation, but the image quality is often degraded. One alternative solution introduced by Wei [23] is to statistically discriminate noise from image edges by a measure based on the local statistical variance of the image. Such a local statistical variance-based edge-stopping algorithm works very well for image restoration. An advantage of this anisotropic diffusion approach is that geometric properties, such as curvature, can be easily embedded in partial differential equation (PDE) operators to achieve desirable effects in image and surface. The level set method devised by Osher and Sethian is a typical example of using the mean curvature flow for image [27–29] and surface analysis [30]. For this reason, this class of nonlinear evolution equations is also called geometric PDEs or geometric flows.

Copyright © 2011 John Wiley & Sons, Ltd.

DOI: 10.1002/cnm

Mathematically, the study of geometric PDEs has enormous impact on geometry analysis, manifold theory, topology, geometric measure theory, and certainly PDEs. In the past two decades, PDE-based image-processing approaches have raised a strong interest in the mathematical community and have opened new approaches for image denoising, enhancement, edge detection, restoration, segmentation, and so forth [3, 30–39]. Recently, geometric PDEs have been utilized as a means for the molecular surface construction of macromolecules [30] and the multiscale modeling of nano-bio systems [40–42].

Variational method is the most powerful mathematical tool. Total variation-based edge-preserving image restoration models were pioneered by Rudin *et al.* [28]. The variational PDE technique has been widely used in numerous applications such as image segmentation [43–45], restoration [28], compression [46], and image inpainting [47]. The growing impact of variational PDE techniques in image processing is mainly due to their capability of controlling the geometrical features of images and data. The essential idea is that signals and images with extra and possibly spurious components have a relatively large variation or gradient. As such, image processing can be formulated as a problem of minimizing the total energy defined as a functional of the gradient of the image, while preserving important image contents such as edges. The minimization of the total energy by the Euler–Lagrange equation leads to a mean curvature term, which helps retain sharp edges in image restoration. Central to most variational PDE methods, the goal of the total energy variation is to reconstruct an image with the best fidelity and the least noise. Regularization procedures and PDE analysis are usually employed in total variation models [48].

Both the Perona–Malik equation [20] and earlier total variation models employ second-order nonlinear PDEs for image or surface analysis. The Willmore flow, proposed in 1920s, is a fourth-order geometric PDE and has also been used for surface analysis. In 1999, Wei introduced the first family of arbitrarily high-order nonlinear PDEs to more efficiently remove image noise in edge-preserving image restoration [23]. The same research group also proposed an arbitrarily high-order geometric PDE for the surface formation and evolution of protein and other molecules [49]. In the past decade, high-order nonlinear PDEs, particularly fourth-order nonlinear PDEs, have attracted much attention in image analysis [21, 23, 48–54]. Compared with second-order PDEs, the higher-order PDEs are able to suppress high-frequency components, including noise, at faster rates. Mathematical analysis of fourth-order nonlinear PDEs in Sobolev space was carried out by Bertozzi and Greer [50, 51, 55], who proved the existence and uniqueness of the solution to a case with H^1 initial data and a regularized operator. Xu and Zhou [56] performed a similar analysis. Recently, Jin and Yang [57] have proved the existence of the strong solution of Wei's fourth-order equation, which is in fact mathematically different from other fourth-order PDEs. In general, however, high-order PDEs are subject to strict stability constraints in their numerical solutions. Witelski and Bowen [58] designed alternating-direction implicit (ADI) schemes for high-order nonlinear PDEs. ADI and other implicit approaches are particularly necessary in signal processing.

Image-processing PDEs of both low-order type and high-order type are mostly designed to function as nonlinear low-pass filters. In 2002, Wei and Jia [24] introduced PDE-based band-pass or high-pass filters for image edge detection. Two evolution PDEs are coupled via relative fidelity terms and the difference of the solutions provides image edges. PDE-based high-pass filters work because when two PDE low-pass filters evolve at dramatically different speeds, the difference of two low-pass PDE operators gives rise to a band-pass filter. The speeds of evolution in the coupled PDEs are controlled by the appropriate selection of their diffusion coefficients. In the extreme case, one can set one of the PDE operator to an identity operator, that is, setting the diffusion and fidelity coefficients to zero. Consequently, one has a PDE-based all-pass filter. The difference between an all-pass filter and a low-pass filter is a high-pass filter [24]. Nonlinear PDE-based edge detection operators have been shown to work extremely well for images with large amount of textures, compared with classical Sobel, Prewitt, and Canny operators [6, 24].

Although nonlinear PDE-based edge detector operators have been introduced for nearly a decade, it was not clear whether PDEs can be utilized to perform all tasks in the image processing for a long time. More specifically, it was not clear whether one can devise PDEs to perform a full-scale mode decomposition. For all practical purposes, the secondary processing becomes easy when all the mode components are available. Therefore, mode decomposition is the real fundamental issue. This

Copyright © 2011 John Wiley & Sons, Ltd.

DOI: 10.1002/cnm

question was not answered until our recent introduction of a family of mode decomposition evolution equations (MoDEEs) [59], which are able to generate various mode components for secondary processing. Similar to wavelets, MoDEEs have controllable time–frequency localization and allow perfect reconstruction, and are thus also called a PDE transform [59]. All of the important building blocks for the PDE transform were developed in our earlier work, that is, arbitrarily high-order PDE filters [23] and PDE-based band-pass or high-pass filters [24]. The PDE transform requires the re-initialization of the initial value in subsequent applications of the PDE operator during the mode decomposition, a procedure inspired by our mode decomposition via iterative filtering [60, 61]. The PDE transform is able to generate physically meaningful modes, also referred to as functional modes. By functional modes, we mean the components that share the same band of frequency as well as same category, that is, trend, edge, texture, noise, and so forth. Obviously, functional modes differ from the pure frequency modes obtained by the Fourier analysis. Based on the functional modes obtained by the PDE transform, secondary processing, or post-processing, can be carried out to achieve desirable processing tasks, such as trend estimation, edge detection, feature extraction, enhancement and denoising, texture analysis, segmentation, and pattern recognition. In fact, the primary and secondary processing are unified in the sense that the same set of PDE transform operators are used with different parameter settings [59].

The objective of the present work is to explore the variational formulation of PDE transforms, to analyze their spectral features, and to consider their biomedical applications. There is no doubt that variational approaches are essential to fundamental sciences, such as physics, mechanics, electrodynamics, chemistry, and biology. As a mathematical tool, variational methods play crucial roles in differential geometry, topology, algebra, PDE, and so forth. Total variation models [28] are the most important ones in image analysis. Therefore, it is useful to investigate the variation formulation of our PDE transform. The present variational PDE transform has to incorporate two unique aspects, namely, high-order nonlinear PDE operators and dynamical coupling of two evolution PDEs. Indeed, the proposed variational formulation of the PDE transform is different from our earlier PDE transforms [59]. Additionally, the Fourier analysis is a valuable approach for the in-depth understanding of the proposed PDE transform. In particular, because of the generality, the proposed PDE transforms appear quite complicated with many parameters. The selection of appropriate PDE transform parameters is nontrivial. Fortunately, the present Fourier analysis sheds light on the behavior of the present PDE transform and thus simplifies the parameter selection. By adjusting the highest order of the PDEs, the proposed PDE transform admits controllable frequency locations, which is desirable in extracting functional modes and closely adjacent frequencies. Finally, the need of technological innovation in biomedical and biological sciences is one of the original motivations for us to design PDE transforms. It is always worthwhile to demonstrate the utility and illustrate the robustness of our new method for practical applications.

The rest of the present paper is organized as follows. Section 2 is devoted to the theory and formulation of PDE transforms. We first review the essence of PDE-based low-pass, band-pass and high-pass filters. We then discuss one form of our earlier PDE transforms. The variational formulation of PDE transforms is proposed in Section 2.4. As mentioned, these new variational PDE transforms have a different structure compared with that of our earlier PDE transforms. The Fourier analysis is carried out in Section 2.5. To simplify our discussion, we consider a high-order linear evolution PDE in one spatial dimension so that the analytical solution can be obtained. Numerical tests and validations are presented in Section 3. High-order PDE transforms are applied to separate two modes with very close frequencies, which is regarded very difficult using other mode decomposition methods. In Section 4, PDE transforms are applied to enhance images obtained with various medical imaging modalities. Such applications include the detection of early lung cancers, noise removal in optical image obtained by the retinal functioning imager, screening of breast cancer using diffuse optical tomography, and image enhancement on electron microscope photography of neuron cells. This paper ends with some concluding remarks.

2. THEORY AND FORMULATION

This section discusses the rationale and variational formulation of PDE transforms. To establish notation and illustrate concepts, we start by a brief review of arbitrarily high-order PDE-based

Copyright © 2011 John Wiley & Sons, Ltd.

DOI: 10.1002/cnm

nonlinear filters introduced by Wei [23]. The central idea is the construction of PDE-based nonlinear high-pass filters introduced by Wei and Jia [24]. We construct PDE transforms by the combination of arbitrarily high-order PDEs and PDE-based high-pass filters. The performance of PDE transforms depends crucially on the use of high-order PDEs in the high-pass filters, which gives rise to the desired frequency localization. In this section, it is also shown that although the exact form of the PDE transform introduced in Ref. [59] can not be derived in a variational formalism, a similar family of PDE transforms can be obtained. The Fourier analysis of a linearized high-order PDE sheds light on the performance of the proposed PDE transform.

2.1. High-order PDE-based low-pass filters

High-order evolution PDEs are widely used in mathematical modeling of material, interface, and curvature [49]. For example, the Willmore flow is often used in the morphological description of membrane. As a high-order generalization of the Perona–Malik equation [20], Wei [23] introduced the first family of arbitrarily high-order nonlinear PDEs for image processing in 1999.

$$\frac{\partial u(\mathbf{r},t)}{\partial t} = \sum_q \nabla\cdot\left[d_q(u(\mathbf{r}),|\nabla u(\mathbf{r})|,t)\nabla\nabla^{2q}u(\mathbf{r},t)\right] + e(u(\mathbf{r}),|\nabla u(\mathbf{r},t)|,t), \quad q=0,1,2,\ldots \tag{1}$$

which has since been applied to image denoising and restoration by many researchers [23,52,62,63]. In Eq. (1), $u(\mathbf{r},t)$ is the image function, and $d_q(u(\mathbf{r}),|\nabla u(\mathbf{r})|,t)$ and $e(u(\mathbf{r}),|\nabla u(\mathbf{r})|,t)$ are the edge sensitive diffusion coefficient and the enhancement operator, respectively. The Perona–Malik equation is recovered at $q=0$ and $e(u(\mathbf{r}),|\nabla u(\mathbf{r})|,t)=0$. As in the original Perona–Malik equation, the hyper-diffusion coefficients $d_q(u(\mathbf{r}),|\nabla u(\mathbf{r})|,t)$ in Eq. (1) can be chosen in many different ways. For instance, one can set

$$d_q(u(\mathbf{r}),|\nabla u(\mathbf{r})|,t) = d_{q0}\exp\left[-\frac{|\nabla u|^2}{2\sigma_q^2}\right], \tag{2}$$

where the values of constants d_{q0} depend on the noise level, and σ_0 and σ_1 are chosen as the local statistical variance of u and ∇u

$$\sigma_q^2(\mathbf{r}) = \overline{|\nabla^q u - \overline{\nabla^q u}|^2} \quad (q=0,1). \tag{3}$$

The notation $\overline{Y(\mathbf{r})}$ above denotes the local average of $Y(\mathbf{r})$ centered at position $\mathbf{r}$. In this algorithm, the statistical measure based on the variance is important for discriminating image edges from noise. As such, one can bypass the image preprocessing, that is, the convolution of the noise image with a test function or smooth mask.

Recently, we have proposed arbitrarily high-order geometric PDEs for surface formation and evolution with application in the surface generation of proteins and other biomolecules [49],

$$\frac{\partial S}{\partial t} = (-1)^q\sqrt{g(|\nabla\nabla^{2q}S|)}\nabla\cdot\left(\frac{\nabla(\nabla^{2q}S)}{\sqrt{g(|\nabla\nabla^{2q}S|)}}\right) + P(S,|\nabla S|), \tag{4}$$

where $S(\mathbf{r},t)$ is a hypersurface function, $g(|\nabla\nabla^{2q}S|) = 1+|\nabla\nabla^{2q}S|^2$ is the generalized Gram determinant, and P is a generalized force term, including the potential interactions that are important to the biomolecular surface formation [49]. When $q=0$ and $P=0$, Eq. (4) reduces to the mean curvature flow equation used in our earlier formulation of minimal molecular surfaces [49], whereas when $q=1$ and $P=0$, it is a surface diffusion flow [49]. Equation (4) can also be regarded as a variation of Wei's earlier arbitrarily high-order PDE (1). The molecular surface generated by Eq. (4) has a distinct morphology [49].

There has been considerable interest in the high-order nonlinear PDE filtering in the past decade [52, 62–64]. The well-posedness of Eq. (1) was analyzed in terms of the existence and uniqueness of the solution by many researchers [50,51,55–57]. In fact, unlike other high-order nonlinear PDEs, Eq. (1) was not derived from a variation formulation. The mathematical properties of the generalized Perona–Malik equation differ from those of other high-order PDEs [57].

Copyright © 2011 John Wiley & Sons, Ltd.

DOI: 10.1002/cnm

2.2. Nonlinear PDE-based band-pass and high-pass filters

Image edge detection and texture extraction require the use of high-pass filters. There are a variety of high-pass filters, including the Sobel, Prewitt, and Canny operators, and discrete singular convolution edge detector [65]. To construct PDE-based edge detectors, Wei and Jia [24] introduced a pair of weakly coupled nonlinear evolution equations,

$$u_t(\mathbf{r},t) = F_1(u, \nabla u, \nabla^2 u, \ldots) + \epsilon_u(v-u), \tag{5}$$

$$v_t(\mathbf{r},t) = F_2(v, \nabla v, \nabla^2 v, \ldots) + \epsilon_v(u-v), \tag{6}$$

where $u(\mathbf{r},t)$ and $v(\mathbf{r},t)$ are scalar fields and ϵ_u and ϵ_v are coupling strengths. In the equations, F_1 and F_2 are general nonlinear diffusion operators and can be chosen as the Perona–Malik operator: $F_1 = \nabla \cdot d_1(|\nabla u|)\nabla$ and $F_2 = \nabla \cdot d_2(|\nabla v|)\nabla$.

The initial values for both scalar fields are chosen to be the same image of interest, that is, $u(\mathbf{r},0) = v(\mathbf{r},0) = X(\mathbf{r})$. In the theory of nonlinear dynamics, Eqs. (5) and (6) constitute a synchronization system. In terms of image processing, Eqs. (5) and (6) are both nonlinear PDE-based low-pass filters. The coupling terms play the role of relative fidelities. To obtain good image edges, two dynamical systems must evolve on the (dramatically) different time scales, that is, $d_{20} \gg d_{10}$. Therefore, when we choose $d_{10} \sim 0$, we have $u(\mathbf{r},t) \sim X(\mathbf{r})$. As such, the coupling terms become the conventional fidelity. In general, low coupling strengths are used so that u or v is mostly modified by the diffusion process during the time evolution and image contrast can be maintained. The image edge was defined as the difference of two diffusion systems [24]

$$w(\mathbf{r},t) = u(\mathbf{r},t) - v(\mathbf{r},t). \tag{7}$$

Equation (7) behaves like a band-pass filter when $d_{20} \gg d_{10} \sim 0$. Without loss of generality, one can set $d_{10} = 0$ [6] and let

$$w(\mathbf{r},t) = X(\mathbf{r}) - v(\mathbf{r},t). \tag{8}$$

where $v(\mathbf{r},t)$ is the solution of

$$v_t(\mathbf{r},t) = F_2(v, \nabla v, \nabla^2 v, \ldots) + \epsilon_v(X-v). \tag{9}$$

Equation (8) works as a PDE-based high-pass filter. The nonlinear PDE-based edge detector described here has been shown to outperform many other classical edge detectors such as Sobel, Prewitt, and Canny operators [24]. An additional important feature of the nonlinear PDE-based edge detector is the ability to extract image texture with high-frequency details [6, 24].

2.3. Partial differential equation transform

The band-pass and high-pass filters described in the previous section do not automatically serve as mode decomposition filters. It takes two more components to perform the mode decomposition. First, commonly used second-order PDE low-pass filters do not have good frequency localization. Consequently, they cannot be directly used for mode decomposition, although they may be utilized in the IFD algorithm as shown in our earlier work [61]. To achieve frequency localization, we have introduced the use of the high-order nonlinear PDEs in our PDE transforms [59]. In general, we can define two nonlinear PDE filters by using the high-order nonlinear PDE operator introduced by Wei [23]

$$\begin{aligned}
&\frac{\partial}{\partial t}\begin{pmatrix} u_m \\ v_n \end{pmatrix} \\
&= \begin{pmatrix} \sum_{j=0}^{m-1} \nabla \cdot d_{uj}(|\nabla u_m|)\nabla\nabla^{2j} - \epsilon_{u_m}(|\nabla u_m|) & \epsilon_{v_n}(|\nabla v_n|) \\ \epsilon_{u_m}(|\nabla u_m|) & \sum_{j=0}^{n-1} \nabla \cdot d_{vj}(|\nabla v_n|)\nabla\nabla^{2j} - \epsilon_{v_n}(|\nabla v_n|) \end{pmatrix} \\
&\quad \times \begin{pmatrix} u_m \\ v_n \end{pmatrix},
\end{aligned} \tag{10}$$

Copyright © 2011 John Wiley & Sons, Ltd.

DOI: 10.1002/cnm

where $\epsilon_{u_m}(|\nabla u_m|)$ and $\epsilon_{u_n}(|\nabla v_n|)$ are made edge sensitive. As low-pass filters, both $d_{uj}(|\nabla u_m|) \geq 0$ and $d_{vj}(|\nabla v_n|) \geq 0$ when j is even. Similarly, both $d_{uj}(|\nabla u_m|) \leq 0$ and $d_{vj}(|\nabla u_m|) \leq 0$ when j is odd. We can define a general edge function as

$$w_{m,n}(\mathbf{r}, t) = u_m(\mathbf{r}, t) - v_n(\mathbf{r}, t) = H_{mn}(\mathbf{r}, t)X(\mathbf{r}), \tag{11}$$

where $H_{mn}(\mathbf{r}, t)$ is a coupled nonlinear PDE operator. For Eq. (11) to work properly, we choose $|d_{vj}(|\nabla v_n|)| \gg |d_{uj}(|\nabla u_m|)|$. As shown in our earlier work, by increasing the order of the highest derivative, one can increase frequency localization and accuracy of the PDE transform for mode decomposition [59]. The frequency selection of $w_{m,n}(\mathbf{r}, t)$ also depends on the evolution time. This aspect is investigated in a later section.

In the PDE transform algorithm, intrinsic mode functions are systematically extracted from residues, that is,

$$w_{mn}^k = H_{mn}X_{mn}^k, \quad \forall k = 1, 2, \ldots \tag{12}$$

where w_{mn}^k is the kth mode function. Here, the residue function is given by

$$X_{mn}^1 = X(\mathbf{r})$$

and

$$X_{mn}^k = X_{mn}^1 - \sum_{j=1}^{k-1} w_{mn}^j, \quad \forall k = 2, 3, \ldots. \tag{13}$$

Therefore, $X = \sum_{j=1}^{k-1} w_{mn}^j + X_{mn}^k$ is a perfect reconstruction of X in terms of all the mode functions and the last residue. The mode decomposition algorithm given in Eq. (12) is essentially nonlinear, even if a linear PDE operator might be used.

2.4. Variational formulation of partial differential equation transforms

Variational models have been extremely successful for a wide variety of science and engineering problems [28, 30, 40–42, 64, 66, 67] and have been an active area of research in applied mathematics. In the field of image analysis, Rudin *et al.* [28] pioneered the total variation-based image restoration models for edge-preserving image denoising. In the present work, we derive a set of high-order nonlinear PDE transforms by variational approach for mode decomposition. Similar variation formulation of high-order nonlinear PDE has been discussed by Didas *et al.* [64]. Let us denote $\mathbf{r} = (x_1, x_2, x_3) \in \mathbb{R}^3$ and define a derivative operator

$$D^j u = \sum_{j_1+j_2+j_3=j} \partial_{x_1}^{j_1} \partial_{x_2}^{j_2} \partial_{x_3}^{j_3} u,$$

where the summation is over all possible nontrivial combinations of $j_1 + j_2 + j_3 = j$. We define the energy functional as

$$E(u, D^1 u, \ldots, D^m u, v, D^1 v, \ldots, D^n v) = \int \left[\Lambda_u \left(\sum_{j=1}^{m} |D^j u|^2 \right) - \Lambda_v \left(\sum_{j=1}^{n} |D^j v|^2 \right) + \epsilon (v - u)^2 \right] \mathrm{d}\mathbf{r}, \tag{14}$$

Copyright © 2011 John Wiley & Sons, Ltd.

DOI: 10.1002/cnm

where $\Lambda_u(\cdot)$ and $\Lambda_v(\cdot)$ are appropriate penalty functions [52, 64]. Minimizing the energy functional (14) by the Euler–Lagrange equation, we have

$$\sum_{j=1}^{m} D^j \Lambda_{uj} \left(\sum_{j=1}^{m} |D^j u|^2 \right) D^j u + \epsilon(v-u) = 0 \tag{15}$$

$$\sum_{j=1}^{n} D^j \Lambda_{vj} \left(\sum_{j=1}^{n} |D^j v|^2 \right) D^j v + \epsilon(u-v) = 0 \tag{16}$$

where $\Lambda_{uj}(\cdot) = (-1)^{j+1} \partial \Lambda_{uj} / \partial D^j u$ and $\Lambda_{vj}(\cdot) = (-1)^{j+1} \partial \Lambda_{vj} / \partial D^j v$.

The energy functional is minimized when Eqs. (15) and (16) are satisfied. To this end, we make use of the steepest descent algorithm with an artificial time and convert Eqs. (15) and (16) into two time dependent PDE transforms

$$\partial_t u = \sum_{j=1}^{m} D^j \Lambda_{uj} \left(\sum_{j=1}^{m} |D^j u|^2 \right) D^j u + \epsilon(v-u) \tag{17}$$

$$\partial_t v = \sum_{j=1}^{n} D^j \Lambda_{vj} \left(\sum_{j=1}^{n} |D^j v|^2 \right) D^j v + \epsilon(u-v). \tag{18}$$

Although the mathematical properties of these high-order PDE transforms may differ from those in Eq. (10), Eqs. (17) and (18) are essentially equivalent to the earlier PDE transforms. Specifically, the magnitudes and signs of Λ_{uj} and Λ_{vj} should be chosen in the same manner as for d_{uj} and d_{vj}, respectively. It is convenient, though not necessary, to set $\epsilon \sim 0$ for mode decomposition. To construct intrinsic mode functions, Eq. (12) is used with the PDE transform operator H_{mn} being replaced by Eqs. (17) and (18).

2.5. *Fourier analysis of partial differential equation transforms*

To analyze the behavior of high-order PDE transforms, let us consider a high-order linear PDE in one spatial dimension

$$\partial_t v = \sum_{j=1}^{n} (-1)^{j+1} d_j \partial_x^{2j} v + \epsilon(X - v), \quad t \geq 0, \tag{19}$$

where $d_j > 0, \epsilon \sim 0$, and X is the initial signal. Equation (19) is subject to initial value $v(x, 0) = X$. The exact solution of Eq. (19) in the Fourier representation is

$$\hat{v}(t) = \hat{L}\hat{X} \tag{20}$$

where $\hat{v}$ and $\hat{X}$ are the Fourier transforms of v and X, respectively. Here $\hat{L}$ is a frequency response function

$$\hat{L}(\epsilon, t, d_1, d_2, \ldots, d_n) = e^{-(\sum_{j=1}^{n} d_j w^{2j} + \epsilon)t} + \frac{\epsilon}{\sum_{j=1}^{n} d_j w^{2j} + \epsilon} \left(1 - e^{-(\sum_{j=1}^{n} d_j w^{2j} + \epsilon)t} \right). \tag{21}$$

As expected, $\hat{L}$ is a low-pass filter. The Fourier representation of the IMF can be given as

$$\hat{w}(t) = \hat{H}\hat{X} \tag{22}$$

where $\hat{H}$ is another frequency response function

$$\hat{H}(\epsilon, t, d_1, d_2, \ldots, d_n) = 1 - e^{-(\sum_{j=1}^{n} d_j w^{2j} + \epsilon)t} - \frac{\epsilon}{\sum_{j=1}^{n} d_j w^{2j} + \epsilon} \left(1 - e^{-(\sum_{j=1}^{n} d_j w^{2j} + \epsilon)t} \right). \tag{23}$$

Copyright © 2011 John Wiley & Sons, Ltd.

DOI: 10.1002/cnm

Obviously, $\hat{H} = 1 - \hat{L}$ is a high-pass filter. The effects of the highest order $2n$, propagation time t, and coupling strength ϵ on the frequency response behavior of high-pass filter $\hat{H}$ is given in Figures 1 and 2. Qualitatively, the behavior of $\hat{L}$ and $\hat{H}$ can be analyzed as $\hat{L}(\epsilon, t, Z) = e^{-Z^2 t} + \frac{\epsilon}{Z}\left(e^{-Z^2 t} - 1\right)$ and $\hat{H}(\epsilon, t, Z) = 1 - e^{-Z^2 t} - \frac{\epsilon}{Z}\left(e^{-Z^2 t} - 1\right)$ where $Z^2 = \sum_{j=1}^{n} d_j w^{2j} + \epsilon$. In particular, the impact of higher order, that is, large $2m$ and $2n$ values, should be examined separately.

It is also interesting to investigate a band-pass filter given by the difference of solutions of two high-order PDEs. To this end, one can simply set $\epsilon = 0$ and define

$$\hat{B}(t, d_{11}, d_{12}, \ldots, d_{1m}, d_{21}, d_{22}, \ldots, d_{2n}) = e^{-(\sum_{j=1}^{m} d_{1j} w^{2j})t} - e^{-(\sum_{j=1}^{m} d_{2j} w^{2j})t}, \tag{24}$$

where we choose $d_{2j} \gg d_{1j} \sim 0$ and $t_2 \geq t_1$. Qualitatively, the behavior of $\hat{B}$ can be analyzed as $\hat{B}(t, Z_m, Z_n) = e^{-Z_m^2 t} - e^{-Z_n^2 t}$ with $Z_n^2 = \sum_{j=1}^{m} d_{2j} w^{2j} \gg Z_m^2 = \sum_{j=1}^{m} d_{1j} w^{2j}$.

In Figures 1 and 2, Fourier analysis for the low-order PDE-based low-pass filter in Eq. (21) and high-pass filter in Eq. (23) is given. We illustrate the control of the frequency localization by parameter $2n$, the highest order of the PDE transform. The effects of coupling strength ϵ (i.e., fidelity term) on the frequency response behavior of the low-pass filter $\hat{L}$ corresponding to the diffusion equation (with $2n = 2$ being the highest-order PDE) are given by the plots in Figure 1(a). The black curve

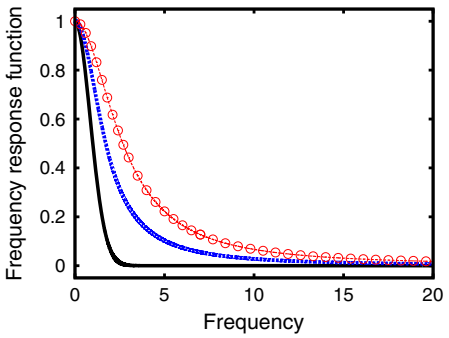

(a) Effect of coupling strength ϵ on the frequency response of the PDE transform low-pass filter in Eq. (23) with $2n = 2$ (and correspondingly $d_1 = 0.14$, $t = 5$). The solid, dashed, circled curves correspond to the same low-pass filter with different values of ϵ=0, 0.4 and 1, respectively.

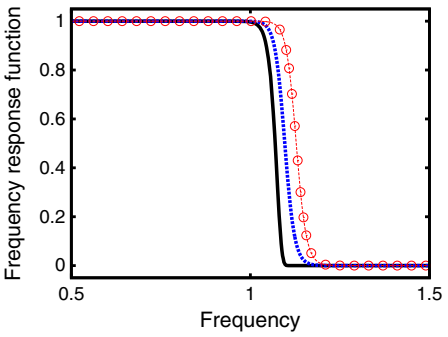

(b) Effect of coupling strength ϵ on the frequency response of the PDE transform high-pass filter in Eq. (23) with $2n = 80$ (and correspondingly $d_{40} = 6.5 \times 10^{-4}$, $t = 5$). The solid, dashed and circled curves correspond to the same low-pass filter with different values of ϵ=0, 1 and 10, respectively.

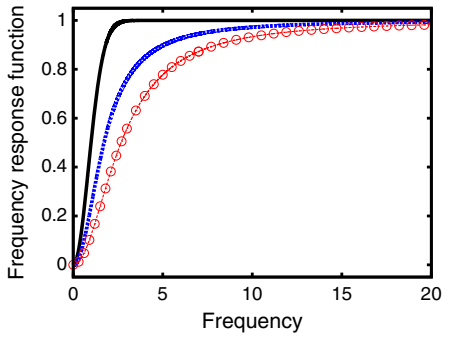

(c) Similar to Figure 1(a) except that the corresponding high-pass filter is shown in this plot.

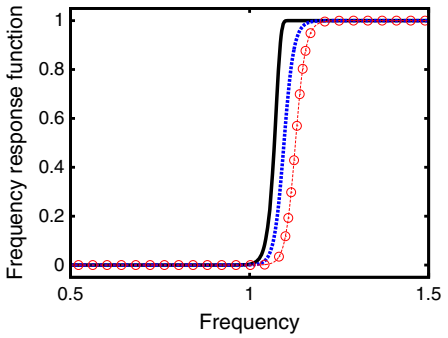

(d) Similar to Figure 1(b) except that the corresponding high-pass filter is shown in this plot.

Figure 1. Fourier analysis of the high-order partial differential equation (PDE)-based low-pass and high-pass filters in Eqs. (21) and (23). Obviously, the time–frequency localization is controlled by parameter $2n$, the highest order of the PDE transform. The effects of coupling strength ϵ (i.e., fidelity term) on the frequency responses $\hat{L}$ and $\hat{H}$ are given. The values of the parameters in Eqs. (21) and (23) are given in the caption below each subfigures.

Copyright © 2011 John Wiley & Sons, Ltd.

DOI: 10.1002/cnm

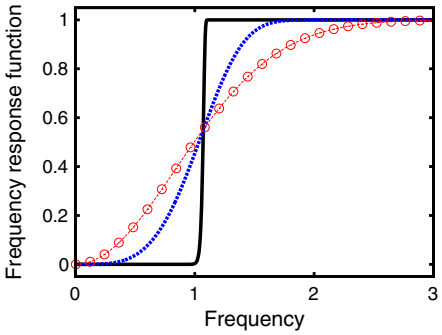

(a) Effect of the highest order of the PDE on the time-frequency localization of the high-pass filter designed in Eq. (23). The value of $2n$ in Eq. (23), which is the highest order of the PDE used, is 2, 4, and 80 for the circled, dashed, and solid curves, respectively, with $d_1 = 0.14$, $d2 = 0.121$, and $d_{40} = 6.5 \times 10^{-4}$. In all the three curves, $\epsilon = 0$ and $t = 5$.

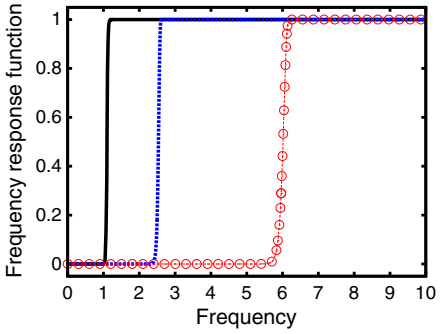

(b) Effect of propagation time on the frequency location (or frequency selection) of the high order PDE filter in Eq. (23). All the three curves show the frequency response functions corresponding to the same value of d_j in Eq. (23) and PDE with same highest order $2n = 80$ and $d_{40} = 6.5 \times 10^{-4}$. In the figure, solid, dashed, and circled lines correspond to the numerical results using propagation time $t = 1, 10^{-30}$, and 10^{-60} respectively.

Figure 2. The control of the time–frequency localization by $2n$ and the frequency location (precision) by t of the high-order partial differential equation (PDE) high-pass filter in Eq. (23).

shows the frequency response of the low-pass filter corresponding to the diffusion equation without fidelity term, that is, $\epsilon = 0$. The blue dashed and red circled curves correspond to the same low-pass filter with different values of $\epsilon = 0.4$ and 1, respectively. If the main purpose of the signal processing is to separate modes with close frequencies, a small ϵ value is preferred. On the other hand, as demonstrated in this paper, higher-order PDEs provide much higher frequency localization and are more efficient in separating modes with closely adjacent frequencies. In Figure 1(b), the highest order of the PDE used is $2n = 80$. The frequency responses approach to the ideal shape of a step function, which provides higher precision in separating modes with closely adjacent frequencies.

The effect of ϵ, however, is different from that in the low-order PDE case. The three curves of black, blue, and red colors are frequency responses of the same low-pass filters with different values of $\epsilon = 0$, 1, and 10. The large coupling strength (i.e., large value of ϵ) does not sacrifice the accuracy of mode decomposition as it does for the low-order PDE; rather, the larger the value of ϵ, the higher shift of the dividing line of the mode frequency separation. In Figures 1(c) and 1(d), the symmetric plots of the high-pass filters are shown corresponding to the low-pass filters in Figures 1(a) and 1(b), respectively.

In Figure 2, the control of the time–frequency localization by $2n$ and the frequency selection by t of the highest order of the PDE on the high-pass filter (23) are explored. The value of $2n$ in Figure 2(a) is equal to 2, 4, and 80 in the red circled, blue dashed, and black solid curves, respectively. As the order increases, the frequency response function becomes steeper and thus represents a better frequency localization, which is needed in the separation of closely adjacent frequency modes. In Figure 2(b) effect of propagation time is examined on the frequency response of the high-order PDE filter in Eq. (23). All the three curves show the frequency response functions corresponding to different values of t with the same PDE. In the figure, black solid, blue dashed, and red circled lines correspond to the numerical results using $t = 1$, 10^{-30}, and 10^{-60}, respectively. Therefore, one can gradually propagate the coupled high-order PDEs in the PDE transform algorithm to systematically extract various modes. The longer propagation time of PDE transforms, the lower frequency of the decomposed mode. The PDE transform algorithm is truly robust and automatic in decomposing signal into series of functional modes or intrinsic modes.

3. NUMERICAL TESTS AND VALIDATIONS

Having analyzed the frequency response of a linear PDE transform, we validate the ability of PDE transform to separate IMFs from signals, and demonstrate such an ability with applications to signals containing closely adjacent frequency modes, which have been practically very challenging.

Copyright © 2011 John Wiley & Sons, Ltd.

DOI: 10.1002/cnm

In Figure 3, the PDE transform is applied to the separation of the three modes (Figure 3(a)) from the signal $\cos(5x) + \cos(1.1x) + \cos(x)$. The highest-order PDE used in the PDE transform is $2n = 32$. The three modes are sequentially separated from the original signal using the same PDE transform algorithm with different values of propagation time t. This is a challenging case due to the extreme closeness of modes $\cos(1.1x)$ and $\cos(x)$. Numerical results for three modes are compared with exact values in Figures 3(b) through 3(d). In Figure 3(b), results for Mode 1, $\cos(5x)$, is shown. The black solid line shows the exact value, and the red circled lines show the numerical values obtained by using the PDE transform algorithm with the 32nd-order PDE. The L_∞ norm of the difference between the exact and numerical curves is negligible (smaller than 10^{-6}). Similarly in Figure 3(c), result of Mode 2, $\cos(1.1x)$, is shown. The L_∞ norm of the difference between the exact and numerical curves is 0.06. In Figure 3(d), results of Mode 3, $\cos(x)$, is shown. The L_∞

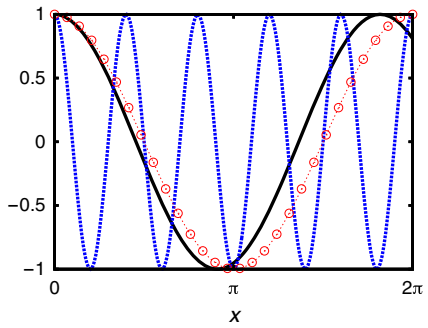

(a) The signal is composed of three frequency modes of $\cos(5x)$, $\cos(1.1x)$, and $\sin(x)$ plotted in dashed, solid and circled lines, respectively.

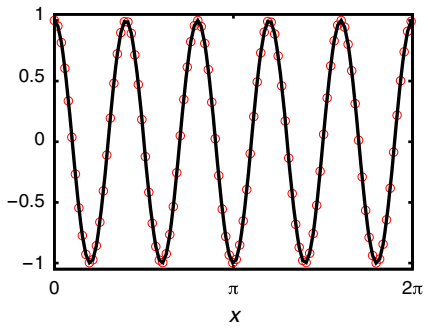

(b) Comparison of numerical results with exact values of Mode 1 of $\cos(5x)$. Solid line shows the exact value, and circled curve shows the numerical values obtained through the PDE transform algorithm using 32nd-order PDE with $d_{16} = -3.5 \times 10^{-22}$ and $t = 5$. The L_∞ norm of the difference between the exact and numerical curves is smaller than 10^{-7}, which is negligible.

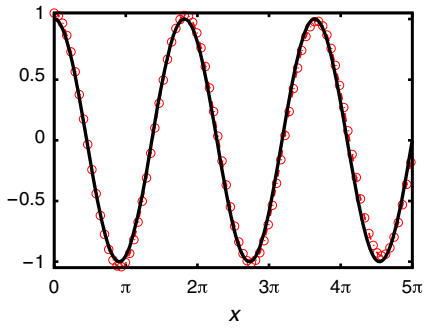

(c) Comparison of numerical results with exact values of Mode 2 of $\cos(1.1x)$. The labels of the curves in this subfigure are same as those in 3(b). Parameters in Eq. (23) are chosen to be $d_{16} = 2.5 \times 10^{-2}$ and $t = 5$. The L_∞ norm of the difference between the exact and numerical curves is 0.06, which is larger than the error for Mode 1 of $\cos(5x)$ in subfigures 3(b) due to the close overlapping of $\cos(1.1x)$ and $\cos(x)$.

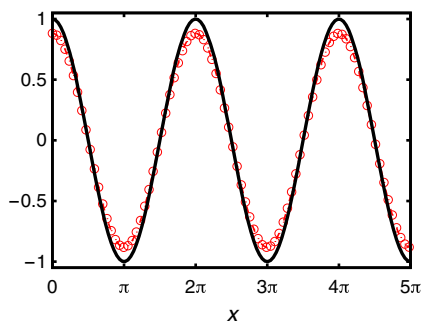

(d) Comparison of numerical results with exact values of Mode 3 of $\cos(x)$. Parameters in Eq. (23) are chosen to be $d_{16} = 10$ and $t = 5$. The L_∞ norm of the difference between the exact and numerical curves is 0.07.

Figure 3. Separation of the three modes from the signal $\cos(5x) + \cos(1.1x) + \cos(x)$ using the partial differential equation (PDE) transform algorithm with the PDE of the highest order of $2n = 32$. The three modes are sequentially separated from the original signal using the same PDE transform algorithm with different propagation time t, respectively.

Copyright © 2011 John Wiley & Sons, Ltd.

DOI: 10.1002/cnm

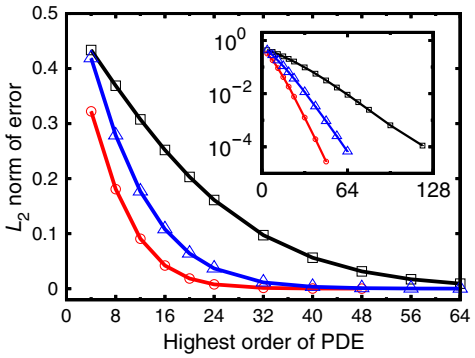

Figure 4. Extraction of higher frequency mode $\sin(mx)$ from the original signal $\sin(x) + \sin(mx)$. In the main window of the figure, x-axis is the highest order of partial differential equation (PDE) employed in the PDE transform algorithm, and y-axis is the L_2 norm error of the high-frequency mode numerically extracted compared with the exact values of $\sin(mx)$. Three different signals of $\sin(x) + \sin(1.1x)$, $\sin(x) + \sin(1.2x)$ and $\sin(x) + \sin(1.3x)$ are decomposed by the PDE transform algorithm, and their numerical results are shown by squared, triangled, and circled curves. The first signal of $\sin(x) + \sin(1.1x)$ with the closest overlapping modes requires much higher order of PDEs to be included in the PDE transform algorithm in order to achieve the same level of accuracy (or error) as for the other two signals. For the purpose of alternative viewing and better understanding, numerical errors are also plotted in log-scale as in the embedded smaller subfigure in the main window above. It is clearly observed that the PDE transform algorithm with higher-order PDE achieves higher accuracy and better resolution in differentiating two modes with closely adjacent frequencies.

norms of the difference between the exact and numerical curves is 0.07 such that two closely adjacent modes $\cos(1.1x)$ and $\cos(x)$ are well separated. Additionally, higher-order PDE can be easily applied to achieve even better accuracy as illustrated in Figure 4.

In Figure 4, convergence is checked with respect to the value of $2n$, which is the highest-order PDE used in the PDE transform. A series of signals are designed as composition of the lower frequency mode $\sin(x)$ with the higher frequency one $\sin(mx)$, where m varies from 1.3 to 1.1 in the figure. In the main window of the figure, x-axis is the highest order of PDE employed in the PDE transform algorithm, and y-axis is the L_2 norm of the error of the high-frequency mode numerically extracted compared with the exact values of $\sin(mx)$. Three different signals of $\sin(x) + \sin(1.1x)$, $\sin(x) + \sin(1.2x)$, and $\sin(x) + \sin(1.3x)$ are decomposed by the PDE transform algorithm. The numerical results are shown by black squared, blue triangled, and red circled curves. The signal $\sin(x) + \sin(1.1x)$ with two closest adjacent modes requires much higher order of PDEs to be included in the PDE transform algorithm in order to achieve the same level of accuracy (or error) as for the other two signals. For example, in order to achieve numerical accuracy with L_2 error bounded below 0.1, a very high-order PDE ($2n = 64$) is required for mode decomposition of the signal with $m = 1.1$ compared with (roughly) 36th-order and 24th-order PDEs needed for signals with $m = 1.2$ and $m = 1.3$, respectively. For better viewing and clearer quantitative comparison, numerical errors are also plotted in log-scale in the embedded small window in Figure 4. It is clearly observed that the PDE transform with higher-order PDE achieves higher accuracy and better resolution in mode decomposition.

More detailed exploration of the convergence of the numerical results shown in Figure 4 is illustrated in Figure 5. The same PDE transform is used to decomposing three signals; $\sin(x)+\sin(1.5x)$, $\sin(x) + \sin(1.5x)$ and $\sin(x) + \sin(1.5x)$ are shown in the first, second, and third rows in Figure 5, respectively. In the first row, the figure on the left shows the numerical results compared with the exact results for the higher frequency mode $\sin(1.5x)$ separated out from the signal using high-pass

Figure 5. Separation of the two modes $\sin(x)$ and $\sin(mx)$, where $m \approx 1$, from the same signal. Convergence of the PDE transform algorithm with various highest-order PDEs are studied. A higher-order PDE transform is needed to differentiate modes with closer frequencies. Propagation time $t = 5$ in all the plots.

Copyright © 2011 John Wiley & Sons, Ltd.

DOI: 10.1002/cnm

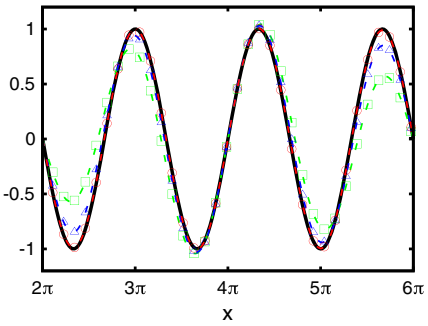

(a) Separation of modes $\sin(1.5x)$ and $\sin(x)$ using the PDE transform. Solid line shows the exact value of $\sin(1.5x)$. Squares, triangles, and circled curves show the numerical results using the highest-order PDE of $2n = 4$, 8, and 16 with $d2 = 0.06$, $d_4 = 0.02$, and $d_8 = 0.002$ respectively.

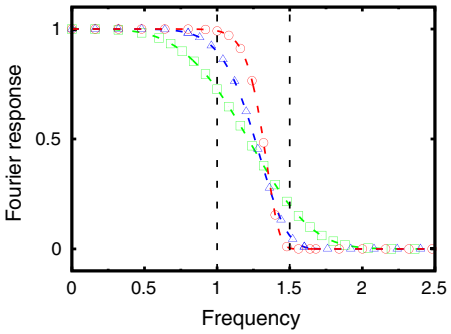

(b) The frequency response of the PDE transform low-pass filters used to obtain results in Figure 5(a). Labels of each curve are same as in Figure 5(a). The two vertical dashed lines correspond to the frequencies of $\sin(x)$ and $\sin(1.5x)$ (i.e. in the Fourier domain), respectively.

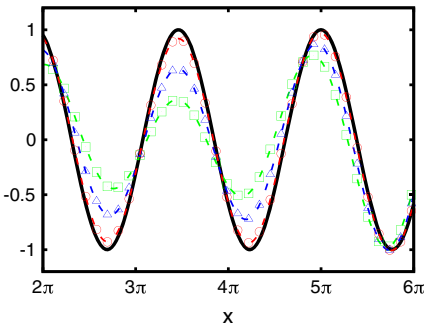

(c) Separation of two modes $\sin(x)$ and $\sin(1.3x)$. Solid line shows the exact value of $\sin(1.3x)$, and squares, triangles, and circled curves show the numerical results using the highest-order PDE of $2n = 4$, 8, and 16 with $d_2 = 0.09$, $d_4 = 0.05$, and $d_8 = 0.01$, respectively.

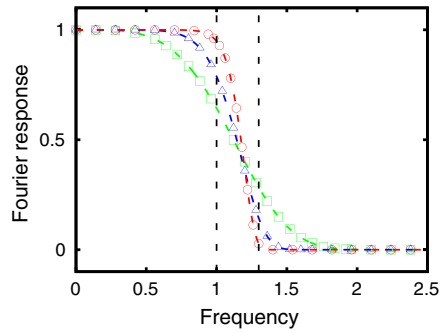

(d) The frequency response of the PDE transform low-pass filters used to obtain results in Figure 5(c). Labels of each curve are the same as in Figure 5(c). The two vertical dashed lines correspond to the frequencies of $\sin(x)$ and $\sin(1.3x)$.

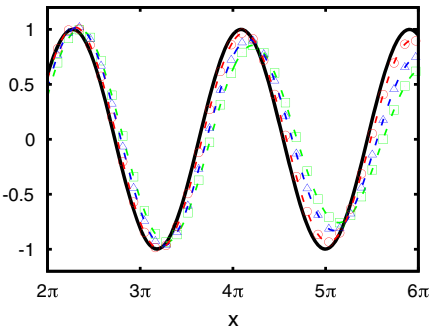

(e) Separation of $\sin(x)$ and $\sin(1.1x)$. Solid line shows the exact value of $\sin(1.1x)$, and squares, triangles and circled curves show the numerical results using the highest order PDE of $2n = 8$, 16 and 32 with $d_4 = 0.1$, $d_8 = 0.07$, and $d_{16} = 0.025$ respectively.

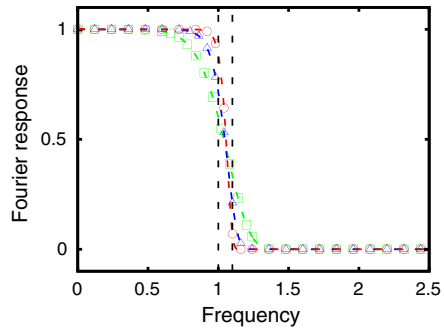

(f) The frequency response of the PDE transform low-pass filters used to obtain results in Figure 5(e). Labels of each curve are the same as in Figure 5(e). The two vertical dashed lines correspond to the frequencies of $\sin(x)$ and $\sin(1.1x)$.

Copyright © 2011 John Wiley & Sons, Ltd.

DOI: 10.1002/cnm

filter designed for the high-order PDE transform algorithm. Exact results are shown by the black curve, whereas green squared, blue triangled, and red circled curves show the numerical results using highest-order PDE with $2n = 4$, 8, and 16, respectively. Similar results are shown in the second row of Figure 5 where the PDE transform is applied to decompose signal $\sin(x) + \sin(1.3x)$. In the third row, because of the closeness of the two modes $\sin(x)$ and $\sin(1.1x)$, higher-order PDEs are required to achieve accurate decomposition. In Figures 5(e) and 5(f), green squared, blue triangled, and red circled curves show the numerical results using highest-order PDE with $2n = 8$, 16, and 32, respectively. For all signals, it is clearly demonstrated that the PDE transform with larger value of n converges better to the exact results. In addition, the figures on the right of all the three rows in Figure 5 show the shape of the frequency responses for the corresponding low-pass filters (i.e., equivalently for the corresponding high-pass filters) designed by the PDE transform algorithm. The larger value of n, the steeper the rising of frequency response functions. In the limit of $n \to \infty$, the frequency response function would become a step function, which ideally divide the frequency domain into high-frequency and low-frequency regions.

Lastly, in Figure 6, the effect of total propagation time t as in Eq. (23) on the frequency response functions is explored in details. The same PDE transform algorithm employing the same highest-order PDE with $2n = 48$ is applied to separate out all the modes from the signal $\sin(x) + \sin(2x) + \sin(3x) + \sin(4x) + \sin(5x) + \sin(6x) + \sin(7x) + \sin(8x) + \sin(9x) + \sin(10x)$. The 10 modes are separated out, in the order of decreasing frequency peak, by varying propagation time t only. When the same set of PDEs composing the PDE transform algorithm are propagated by $t = 4.3 \times 10^{-48}$, the highest-frequency mode $\sin(10x)$ is decomposed; after another propagation time $t = 9.4 \times 10^{-46}$, the next highest-frequency mode $\sin(9x)$ is decomposed, and so on. It is worthwhile to point out that, though the propagation time ranges from 10^{-50} to 1, no specific temporal discretization is needed in the current PDE scheme because the time integral is numerically calculated using one time step. In Figure 6(b), values of propagation time t are plotted as the function of the frequency peaks of the modes being decomposed. The numerical values of t (labeled by

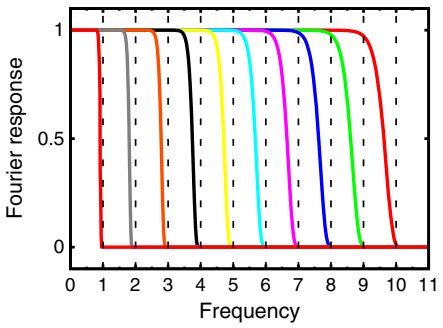

(a) The curves from left to right correspond to the frequency responses of low-pass filters (which are the Fourier transform of PDEs in the PDE transforms) applied to separate 10 modes of $\sin(x)$, $\sin(2x)$, ... and $\sin(10x)$ consecutively. The frequency response curves are generated using different values of propagation time growing from $t \approx 10^{-50}$ to $t \approx 10^{0}$. The exact corresponding values of propagation time is shown in Figure 6(b). For reference, frequencies of each of the 10 modes in the frequency space are indicated by the vertical black dashed lines.

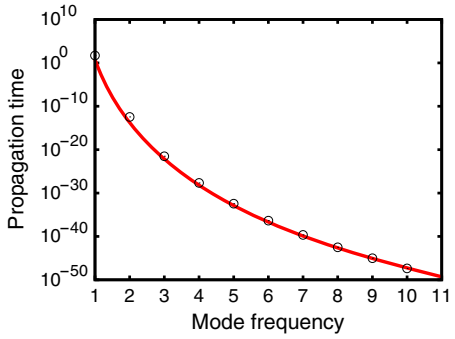

(b) Total effective propagation time τ in the PDE transform, where τ is the product of super diffusion constant and actual physical propagation time t. In the simplest case of the PDE transform with the highest PDE of 2nd order only, i.e., the diffusion equation, τ is the product of diffusion constant D and propagation time t. In the figure, the horizontal axis is the location of mode in frequency space, e.g., mode frequency of $\sin(3x)$ is 3. The curve is the analytical plot for $1/w^{48}$ which approximately fits the numerical values labeled by circles.

Figure 6. Mode decomposition of the signal $\sin(x) + \sin(2x) + \sin(3x) + \sin(4x) + \sin(5x) + \sin(6x) + \sin(7x) + \sin(8x) + \sin(9x) + \sin(10x)$ using the partial differential equation (PDE) transform algorithm including PDE terms up to the 48th order with $d_{24} = 1$. The figure indicates that separation of lower frequency mode requires larger effective propagation time τ, or equivalently speaking larger effective diffusion constant.

Copyright © 2011 John Wiley & Sons, Ltd.

DOI: 10.1002/cnm

the black circles) fits well into the analytical estimation $1/w^{48}$ shown by the red solid curve, where the value of 48 corresponds to the value $2n = 48$ of the highest-order PDE used herein.

The PDE transform algorithm has been designed for the mode decomposition of arbitrary dimensional signals or images. In previous Figures, one-dimensional (1D) signals have been used for illustration and validation purposes. In Figure 7, a two-dimensional (2D) signal $\sin(4x)\sin(2y) + \sin(4.2x)\sin(2.2y)$ is decomposed by the PDE transform algorithm into the two

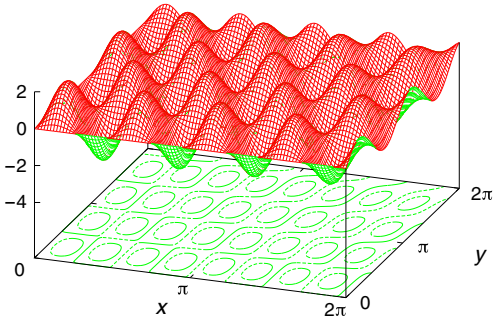

(a) Two-dimensional signal $\sin(4x)\sin(2y) + \sin(4.2x)\sin(2.2y)$. The contour plot for the 2D signal is projected on the base of the above subfigure.

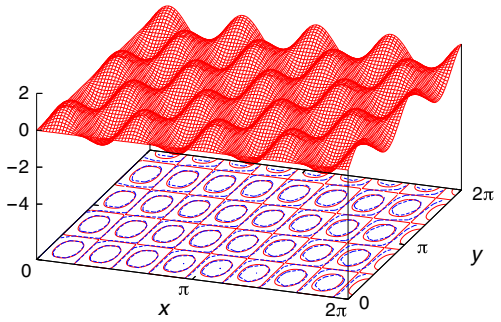

(b) High frequency mode $\sin(4.2x)\ \sin(2.2y)$. The L_2 error of the PDE transform results compared to the exact values is 0.11. To differentiate the small difference between numerical results and exact values, contour plots for both surfaces are projected together on the base. The red and blue colors indicates the contour plots of the PDE transform and exact results, respectively.

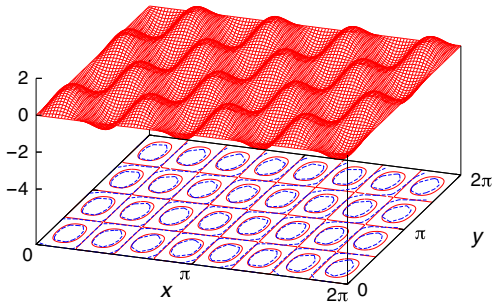

(c) Low frequency mode $\sin(4x)\sin(2y)$. Same labels and color sets as in subfigure 7(b) are used for differentiating the contour plot for the PDE transform results from that for the exact mode.

Figure 7. Mode decomposition of the signal $\sin(4x)\sin(2y)+\sin(4.2x)\sin(2.2y)$ using the partial differential equation (PDE) transform algorithm including PDE terms up to the eighth order. Results of two modes $\sin(4.2x)\sin(2.2y)$ and $\sin(4x)\sin(2y)$ are shown in subfigures 7(b) and 7(c), respectively.

Copyright © 2011 John Wiley & Sons, Ltd.

DOI: 10.1002/cnm

modes $\sin(4x)\sin(2y)$ and $\sin(4.2x)\sin(2.2y)$. A relatively low value of $2n = 16$ for the highest-order PDE is sufficient to achieve good enough numerical results of decomposed signal. L_2 norm error is 0.1 compared with the amplitude 2.0. By increasing value $2n$ of the highest-order PDEs employed in the PDE transform algorithm, similar convergence can be achieved as for the 1D signals. The PDE transform algorithm has been designed to work naturally and equally efficient for arbitrarily dimensional signals and images.

4. APPLICATIONS TO BIOMEDICAL AND BIOLOGICAL IMAGES

In this section, we apply the PDE transform algorithm to several different types of medical images for image denoising and enhancement.

4.1. Early cancer detection

In the initial period of the cancer development, the patient may not exhibit noticeable symptoms such that it would be too late even if they quickly pick up alerting messages when the cancer has developed for some time already. It is critical to detect cancer in its early state in order to provide a successful cure or surgery. Various medical imaging techniques have been developed to help diagnose and detect cancer. In addition to the hardware-type imaging techniques, image post-processing can be applied to render a clearer image showing the important details of the cancer images. In this section, imaging techniques and processing are discussed with application to lung cancer and breast cancer.

The general technique for early lung cancer is screening chest with X-ray or spiral computed tomography scan. Such a technique is useful for detecting the lung cancer in its more localized phase, which implies that it is more likely to be curable. One important goal of imaging and image processing is to decide whether the tumor is resectable and whether it should be a lobectomy or a pneumonectomy. Lobectomy means surgical excision of a lobe of the lung. On the other hand, a pneumonectomy is a surgical procedure to remove the whole lung. Clearly the lobectomy approach is a better and safer choice than pneumonectomy if the former is possible. The restriction for performing a lobectomy of the lung is that the surgery can not be performed on patients with lung cancers spreading to other parts of the tissue. Details from the medical images are therefore helpful in making the decision. In medical imaging or internal organs or brain, pictures are usually taken along one or many of the three planes (see Figure 8): axial plane, which refers to the slice parallel to the feet of the patient; coronal plane, which is the slice perpendicular to the feet and parallel to the shoulder line of the patient; and sagittal plane, which is the vertical plane passing from front to rear and dividing the body into right and left sections. Images taken on the three planes together give

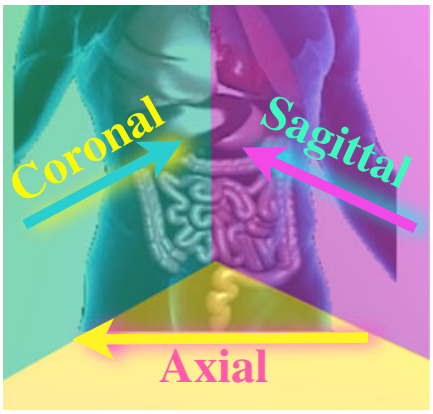

Figure 8. The axial plane is an imaginary plane that divides the body into superior and inferior parts. A coronal plane divides the body into back and front portions. A sagittal plane is a vertical plane that passes from front to rear dividing the body into right and left sections. The three planes are perpendicular to each others.

Copyright © 2011 John Wiley & Sons, Ltd.

DOI: 10.1002/cnm

three-dimensional information of the internal organ of the human body. In Figures 9(e) and 9(f), images of the patient's lung taken along the axial and coronal planes are shown, respectively. To test the effect of the PDE transform algorithm, random (Gaussian-type) noise are added in Figures 9(a) and 9(b). The PDE transform algorithm with up to fourth-order PDE is used to smooth and enhance the images, results of which are shown in Figures 9(c) and 9(d). In the axial image (Figure 9(c)), one can see the shape of the tumor near the fissure on the left. However, this information alone is not enough for making decision whether the tumor is resectable and whether it should be a lobectomy or a pneumonectomy. The image in Figure 9(d) taken along the coronal plane clearly shows there is no transfissural growth. As such, the tumor is localized and does not cross the fissure, which divides the superior lobe from the middle lobe. Therefore lobectomy is a possibility. The lung of another patient is imaged along the coronal and sagittal planes as shown in Figure 10. Similarly, white noise is added to the images, and the PDE transform algorithm with up to the fourth-order PDE is performed to smooth the images. Comparing Figure 9(c) with Figure 10(c), transfissural growth is observed in the latter case. The picture taken along the sagittal plane in Figure 10(d) further demonstrates that the tumor crosses the horizontal fissure of the lung. Therefore, lobectomy is not possible according to the images shown in these Figures.

Detection of breast cancer is another important application of medical imaging and image processing. One of the widely used exams for early detection of breast cancer is mammogram, which take picture of breast with a safe, low-dose X-ray machine. Diffuse optical tomography (DOT) has recently been used to create high-resolution images from a scattering of infrared and visible light for the early detection of breast cancer. DOT is a three-dimensional method where photon density waves are launched from a source and then travel in a banana-shaped path due to multiple scattering, which is different from the straight paths followed by X-rays in mammogram. Compared to the use of X-rays in mammogram imaging, DOT is relatively less expensive, safer and more comfortable. However, the photon density waves used in DOT are more difficult to track because of the scattering and absorption. Image processing is usually performed to remove noise and enhance image quality. In Figure 12(a), a high-resolution image is shown created by the DOT technology. The distorted region in the black circle in the image indicates the area of abnormalities associated with the breast cancer. Image shown in Figure 12(b) contains combination of two types of noises: highly oscillatory random noises (with up to 200 oscillations in each direction of the 256×256-pixel image and with random amplitude in each oscillation) and Gaussian-type random noise with standard deviation equal to 30 (see Figure 12(d)). The fine lines of image are therefore distorted and contaminated. In Figure 12(c), an enhanced image is generated from Figure 12(b) by applying the PDE transform algorithm using up to the fourth-order PDE. The fine details are well recovered. Such image enhancement can be combined with other mathematical models in development by other groups to make the DOT a better imaging techniques for detecting smaller breast cancer with lower cost and higher safety and reliability.

4.2. Optical images from retinal functioning imager

Besides the important biological function of vision, eyes are also helpful for the diagnosis of diseases such as diabetes as well as for the assessment and identification of various neurological effects. A number of technological progresses has advanced the retinal imaging for research and clinical applications, for example. Many imaging techniques including retinal function imager (RFI), positron emission tomography (PET), and functional magnetic resonance imaging (fMRI) have been developed to provide high-resolution images. In particular, RFI is an adaptive noninvasive approach to study the single red blood cells moving through capillaries [68, 69], and it enables direct visualization of retinal blood dynamics without the injection of contrast agents. The motion of individual red blood cells and blood cell clusters can be revealed with much clarity, which is important towards the quantitative detection of abnormal blood flow velocity in capillaries and arterioles. Like many other medical imaging techniques, poor signal-to-noise ratio in *in-vivo* applications is always a concern. Various post-image-processing techniques are generally applied to render enhanced images. In Figure 11, qualitative oximetry with the RFI is applied to detect the perfusion deficits and abnormalities in a patient with sickle cell retinopathy. The area with abnormalities appear as regions of gray scale

Copyright © 2011 John Wiley & Sons, Ltd.

DOI: 10.1002/cnm

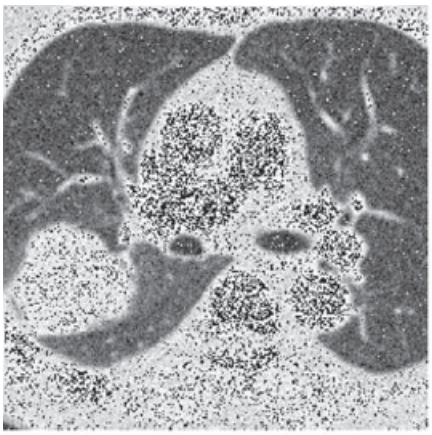

(a) Axial image of the lung.

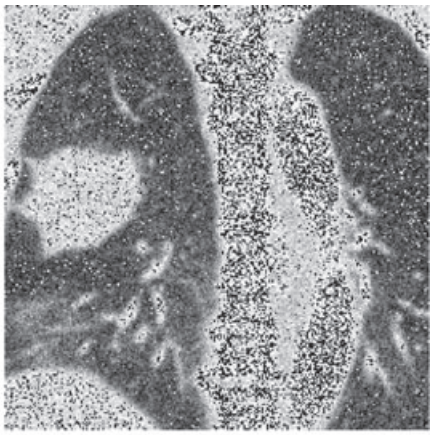

(b) Coronal image of the lung.

(c) Denoised axial image showing a tumor near the fissure on the left.

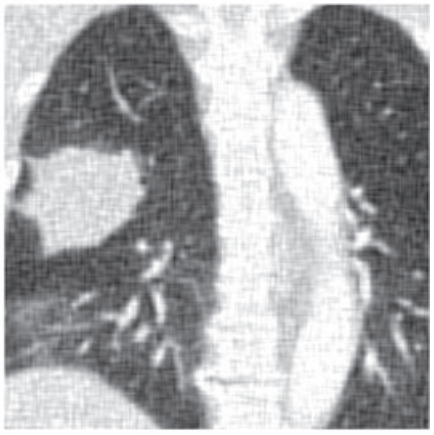

(d) Denoised coronal image demonstrating that there was no transfissural growth of the tumor.

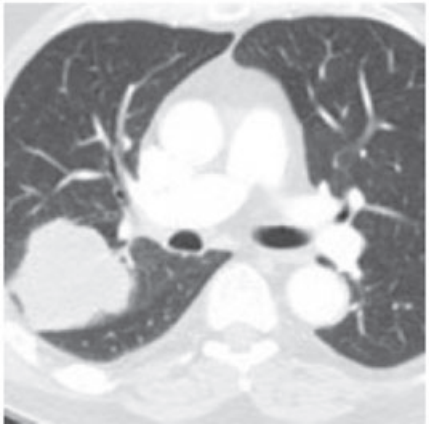

(e) Original noise-free axial image of the lung.

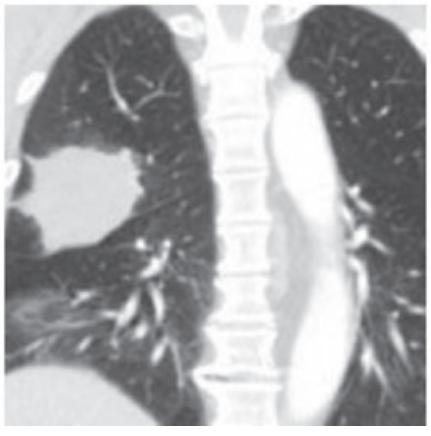

(f) Original noise-free coronal image of the lung.

Figure 9. Partial differential equation transform algorithm using up to fourth-order PDE is used to denoise and enhance the images for lung diagnosis. The tumor is detected in the axial image, and the details shown in the coronal image demonstrates that there was no transfissural growth of the tumor such that lobectomy surgical excision of a lobe only is possible.

Copyright © 2011 John Wiley & Sons, Ltd.

DOI: 10.1002/cnm

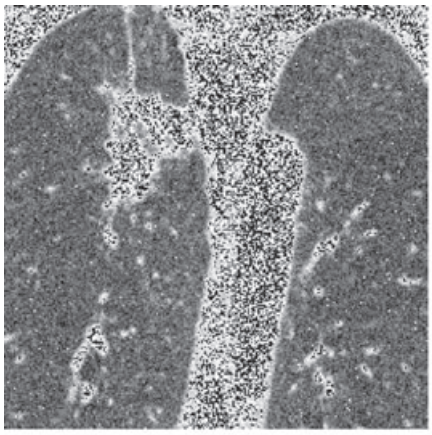

(a) Coronal image of the lung.

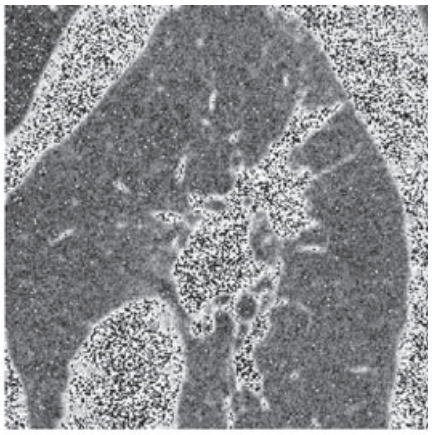

(b) Sagittal image of the lung.

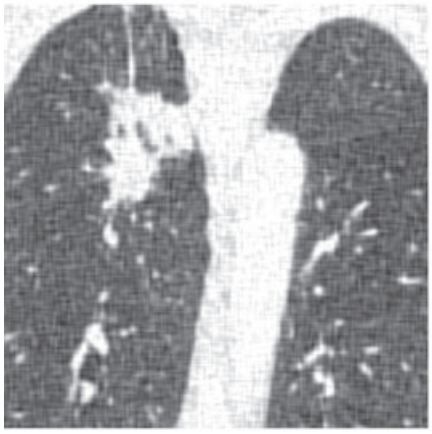

(c) Denoised coronal image showing that tumor is present and is transfissural.

(d) Denoised sagittal image further revealing the details of the transfissual growth of the tumor.

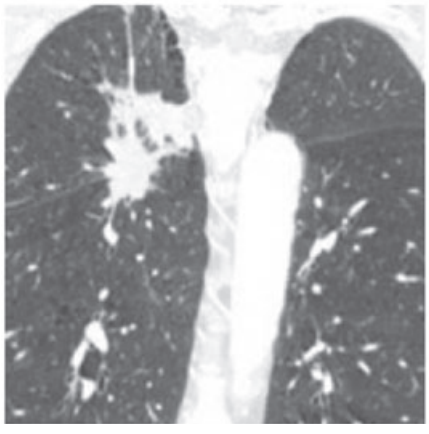

(e) Original noise-free coronal image of the lung.

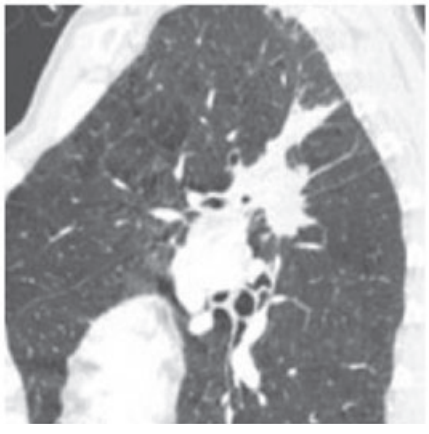

(f) Original noise-free sagittal image of the lung.

Figure 10. Partial differential equation transform algorithm using up to fourth-order PDE is used to denoise and enhance the images for lung diagnosis. The coronal image shows that there was transfissural growth of the tumor, and the sagittal image reveals more details supporting the diagnosis that lobectomy surgical excision of a lobe only is not possible and pneumonectomy is a surgical procedure might be needed to remove the whole lung.

Copyright © 2011 John Wiley & Sons, Ltd.

DOI: 10.1002/cnm

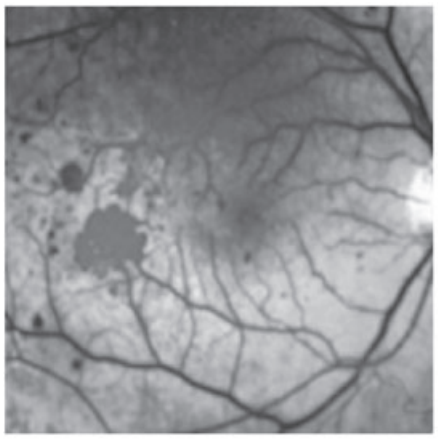

(a) Optical images from retinal functioning imager (RFI) for a patient with sickle cell retinopathy. The area with abnormalities appear as regions of grey scale distinct from their surroundings.

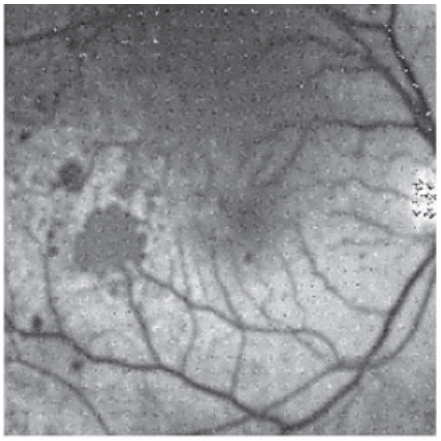

(b) Locally distributed white noise is added to the original image in Figure 11(a) to mimic the RFI noise in the real experiments.

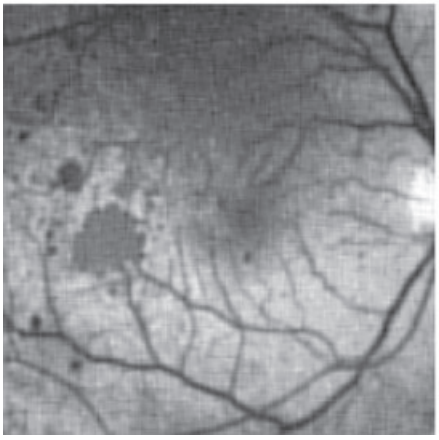

(c) Denoised image using the PDE transform algorithm with the second order PDE.

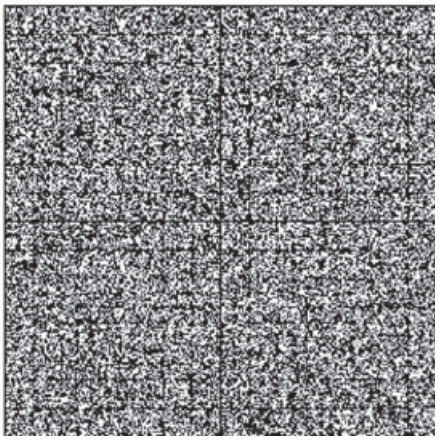

(d) The image showing the noise added to the original image, which is composed of both Gaussian white noise and highly oscillatory random noise.

Figure 11. Using qualitative oximetry with optical images from a retinal function imager (RFI), perfusion deficits and abnormalities in a patient with sickle cell retinopathy is detected. The partial differential equation (PDE) transform algorithm using up to the fourth-order PDE is used to denoise and enhance the RFI images.

distinct from their surroundings. Figure 11(a) shows a high-resolution image with good resolution. In Figure 11(b), noise is added, which is composed of both a highly oscillatory noise (with up to 30 oscillations in each direction of the 256×256-pixel image) with random amplitudes and Gaussian-type random noise (with standard deviation equal to 30). The PDE transform algorithm using up to fourth-order PDE is applied for denoising the image. Result is shown in Figure 11(c). Such image enhancement technique would be useful in further improving the image quality of high-resolution RFI.

4.3. Electron microscope photography of neuron systems

With an intricately elaborate dendritic arbor, Purkinje neurons are characterized by a large number of dendritic spines. Purkinje neurons are some of the largest of the 100 billion neurons in the human brain. Neuron cells are the masters of motor coordination in the cerebellar cortex. These large dendritic arbors form nearly 2D layers through which parallel fibers from the deeper layers pass. Toxic

Copyright © 2011 John Wiley & Sons, Ltd.

DOI: 10.1002/cnm

(a) High-resolution image created by diffuse optical tomography. The distorted region in the black circle is the area of abnormalities, which is the breast cancer in this case.

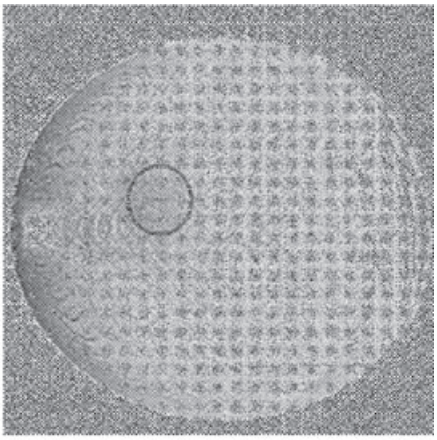

(b) The original image is contaminated with highly oscillating and random noise in Figure 12(d).

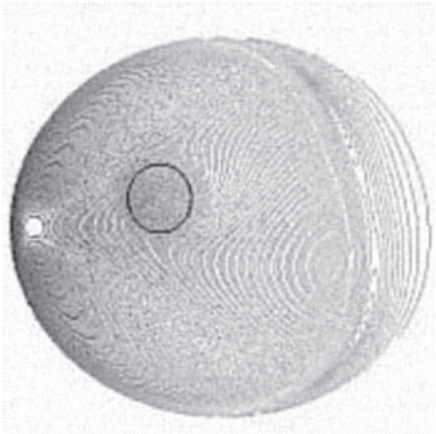

(c) Denoised image using the PDE transform algorithm. All the fine details and area of abnormalities are recovered from the noise.

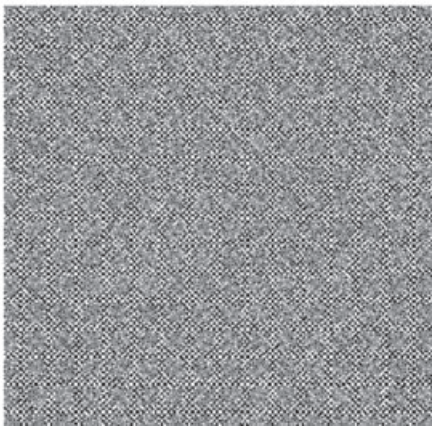

(d) Image showing the noise added to Figure 12(a). The random noise is similar to that in Figure 11(d) except that two different types of highly oscillatory noises are embedded in the Gaussian noise to make the denoising more challenging.

Figure 12. Diffuse optical tomography is used to create extremely high-resolution images from a scattering of infrared and visible light. Such technology can be used for the early detection of breast cancer. As light travels from the source, once it hits the black circle where the tumor is located, the lightwaves become distorted. One practical challenge is that the high-resolution imaging is subjected to noises, especially highly oscillatory noise, which would distort the fine details in the image. The partial differential equation (PDE) transform can be used to smooth the image and is particularly good for removing high-frequency noise and/or oscillatory noises.

exposure to such as alcohol and lithium and various immune or neurodegenerative diseases such as autism and Alzheimer's disease can negatively affect human Purkinje cells and their shape and structure. Therefore, a clear visualization of the detailed shape of Purkinje neurons would be useful in the study and diagnosis of various diseases. In Figure 13, electron microscope photography of Purkinje neurons is shown. Electron microscope is a type of microscope that uses a particle beam of electrons to illuminate the sample and to generate a magnified image. Electron microscopes usually have a greater resolving power than a light-powered optical microscope because of the much smaller wavelength of electrons. Using electron microscope imaging technique, the details of vast amount of dendrites on the neuron cells can be highlighted and explored. Noise removal using image processing can further provide a better quality image. The PDE transform using up to the fourth-order PDE is used to denoise the image in Figure 13(b) to generate a better resolved one in Figure 13(c) in

Copyright © 2011 John Wiley & Sons, Ltd.

DOI: 10.1002/cnm

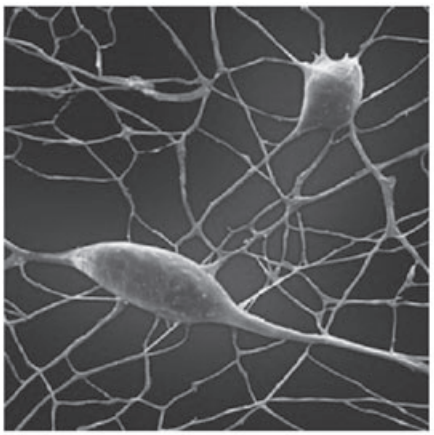

(a) Purkinje neurons are some of the largest of the 100 billion neurons in human brain.

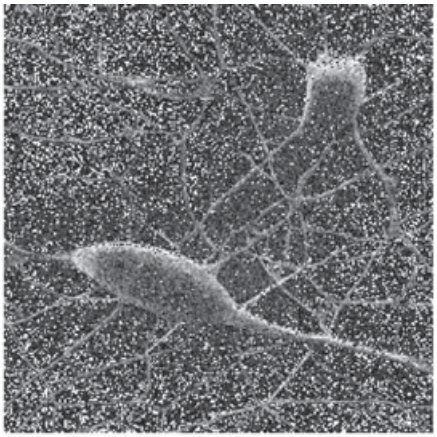

(b) The original image is contaminated with highly oscillatory and random noise in Figure 13(d).

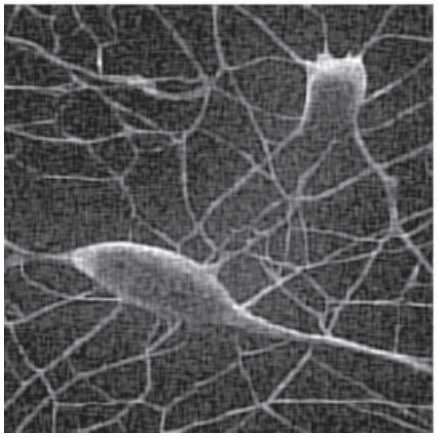

(c) Denoised image using the PDE transform algorithm. Both the shapes and details of dendrites are well recovered from the noise-contaminated image.

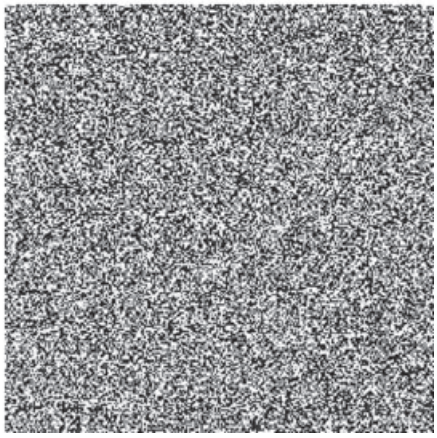

(d) Image showing the random noise added to Figure 13(a).

Figure 13. Electron microscope photography of Purkinje neurons showing the details of vast amount of dendrites on the neuron cells. The partial differential equation transform using up to the fourth-order PDE is used to denoise the image and enhance the details of cell structure and geometry details of the dendrites.

which the details of cell structure and geometry of the dendrites are better rendered compared with the original high-resolution picture in Figure 13(a).

5. CONCLUDING REMARKS

Geometric PDEs are of tremendous importance in signal and image processing, data analysis, and surface construction. Mode decomposition is an elementary process in a variety of signal/image-processing tasks. However, despite the great progresses made in geometric PDEs accompanying the broad interests in the past two decades, the use of geometric PDEs for mode decomposition was not realized until a recent advance in the field. The resulting models, called PDE transform, has been introduced in our earlier work [59] based on arbitrarily high-order nonlinear PDE introduced by Wei [23] and PDE-based image edge operator introduced by Wei and Jia [24]. The present work introduces the variational formulation, provides the Fourier analysis, and carries out the biomedical and biological applications of the PDE transform.

In the variational formulation of PDE transform, we construct a total energy functional consisting of two image functions and two sets of geometric operators. Because of the dynamical coupling

Copyright © 2011 John Wiley & Sons, Ltd.

DOI: 10.1002/cnm

of two operators, the relative signs of two operators are different, which contributes to the energy disparity. The dynamical coupling of two image functions reduces the energy disparity. The energy minimization by using the Euler–Lagrange equation and the introduction of artificial propagation time by the steepest descent algorithm lead to a system of two coupled nonlinear PDE transforms. As discussed in our earlier work [23], these two equations have to evolve at dramatically different time scales to generate sufficient disparity in the two image functions. Their difference corresponds to the desirable intrinsic mode functions when appropriate model parameters and initial values are provided. To aid the parameter selection, we carried out detailed Fourier analysis on a prototype linear PDE transform, which admits an analytical solution in the Fourier domain. As such, we analyze the filter properties of arbitrarily high-order PDE transforms. This analysis provides a guidance for the parameter selection of the proposed PDE transforms. For instance, the order of the highest PDE can be selected to control the frequency localization, whereas the propagation time or the amplitude of diffusion coefficients of the PDE transform can be adjusted to control the frequency location or precision. Many challenging test examples are explored to validate the proposed PDE transforms for decomposing intrinsic mode functions. We demonstrate usefulness of the proposed PDE transforms by biomedical and biological applications. Image denoising, enhancement, and restoration are considered in the present work for early lung cancer detection, optical image, diffuse optical tomography, and electron microscope photography. Numerical experiments indicate that the proposed PDE transform works well.

ACKNOWLEDGEMENTS

This work was supported in part by NSF grants CCF-0936830 and DMS-1043034, NIH grant R01GM-090208, and MSU Competitive Discretionary Funding Program grant 91-4600.

REFERENCES

1. Chan YT. *Wavelet basics*. Springer, 1995.
2. Farge M. Wavelet transforms and their applications to turbulence. *Annual Review of Fluid Mechanics* 1992; **24**:395–457.
3. Sazonov I, Yeo SY, Bevan RLT, Xie XH, van Loon R, Nithiarasu P. Modelling pipeline for subject-specific arterial blood flow—a review. *International Journal for Numerical Methods in Biomedical Engineering* in press, 2011:1–46.
4. Spedding GR, Browand FK, Huang NE, Long SR. A 2-d complex wavelet analysis of an unsteady wind-generated surface-wave field. *Dynamics of Atmospheres and Oceans* 1993; **20**(1-2):55–77.
5. Gu Y, Wei GW. Conjugate filter approach for shock capturing. *Communications in Numerical Methods in Engineering* 2003; **19**(2):99–110.
6. Sun YH, Wu PR, Wei G, Wang G. Evolution-operator-based single-step method for image processing. *International Journal of Biomedical Imaging* 2006; **83847**:1.
7. Sun YH, Zhou YC, Li SG, Wei GW. A windowed Fourier pseudospectral method for hyperbolic conservation laws. *Journal of Computational Physics* 2006; **214**(2):466–490.
8. Zhao S, Wei GW. Jump process analysis for the trend estimation of time series. *Computational Statistics and Data Analysis* 2003; **42**:219–241.
9. Liang HL, Lin QH, Chen JDZ. Application of the empirical mode decomposition to the analysis of esophageal manometric data in gastroesophageal reflux disease. *IEEE Transactions on Biomedical Engineering* 2005; **52**(10):1692–1701.
10. Oppenheim AV, Schafer RW. *Digital Signal Process*. Prentice-Hall: Englewood Cliffs, NJ, 1989.
11. Titchmarsh EC. *Introduction to the Theory of Fourier Integrals*. Oxford University Press, 1948.
12. Daubechies I. *Ten Lectures on Wavelets*. SIAM: Philadelphia, 1992.
13. Guan S, Lai CH, Wei GW. A wavelet method for the characterization of spatiotemporal patterns. *Physica D: Nonlinear Phenomena* 2002; **163**(1-2):49–79.
14. Jin JH, Shi JJ. Feature-preserving data compression of stamping tonnage information using wavelets. *Technometrics* 1999; **41**(4):327–339.
15. Mallat S. *A Wavelet Tour of Signal Processing*. Academic Press, 1999.
16. Meyer FG, Coifman RR. Brushlets: a tool for directional image analysis and image compression. *Applied and Computational Harmonic Analysis* 1997; **4**(2):147–187.
17. Wei GW. Wavelets generated by using discrete singular convolution kernels. *Journal of Physics A: Mathematical and General* 2000; **33**:8577–8596.
18. Huang NE, Long SR, Shen Z. The mechanism for frequency downshift in nonlinear wave evolution. *Advances in Applied Mechanics* 1996; **32**:59.

Copyright © 2011 John Wiley & Sons, Ltd.

DOI: 10.1002/cnm

19. Witkin A. Scale-space filtering: a new approach to multi-scale description. In *Proceedings of IEEE International Conference on Acoustic Speech Signal Processing*, Vol. 9, Institute of Electrical and Electronics Engineers, 1984; 150–153.
20. Perona P, Malik J. Scale-space and edge-detection using anisotropic diffusion. *IEEE Transactions on Pattern Analysis and Machine Intelligence* 1990; **12**(7):629–639.
21. Chan T, Marquina A, Mulet P. High-order total variation-based image restoration. *SIAM Journal on Scientific Computing* 2000; **22**(2):503–516.
22. Soltanianzadeh H, Windham JP, Yagle AE. A multidimensional nonlinear edge-preserving filter for magnetic-resonance image-restoration. *IEEE Transactions on Image Processing* 1995; **4**(2):147–161.
23. Wei GW. Generalized Perona–Malik equation for image restoration. *IEEE Signal Processing Letters* 1999; **6**(7):165–167.
24. Wei GW, Jia YQ. Synchronization-based image edge detection. *Europhysics Letters* 2002; **59**(6):814–819.
25. Catte F, Lions PL, Morel JM, Coll T. Image selective smoothing and edge-detection by nonlinear diffusion. *SIAM Journal on Numerical Analysis* 1992; **29**(1):182–193.
26. Nitzberg M, Shiota T. Nonlinear image filtering with edge and corner enhancement. *IEEE Transactions on Pattern Analysis and Machine Intelligence* 1992; **14**(8):826–833.
27. Osher S, Sethian JA. Fronts propagating with curvature-dependent speed: algorithms based on Hamilton–Jacobi formulations. *Journal of computational physics* 1988; **79**(1):12–49.
28. Rudin LI, Osher S, Fatemi E. Nonlinear total variation based noise removal algorithms. *Physica D* 1992; **60**(1-4):259–268.
29. Sethian JA. Evolution, implementation, and application of level set and fast marching methods for advancing fronts. *Journal of Computational Physics* 2001; **169**(2):503–555.
30. Bates PW, Wei GW, Zhao S. Minimal molecular surfaces and their applications. *Journal of Computational Chemistry* 2008; **29**(3):380–391.
31. Barbu T, Barbu V, Biga V, Coca D. A PDE variational approach to image denoising and restoration. *Nonlinear Analysis Real World Applications* 2009; **10**(3):1351–1361.
32. Bertalmio M. Strong-continuation, contrast-invariant inpainting with a third-order optimal PDE. *IEEE Transactions on Image Processing* 2006; **15**(7):1934–1938.
33. Caselles V, Morel JM, Sapiro G, Tannenbaum A. Introduction to the special issue on partial differential equations and geometry-driven diffusion in image processing and analysis. *IEEE Transactions on Image Processing* 1998; **7**(3):269–273.
34. Grimm V, Henn S, Witsch K. A higher-order PDE-based image registration approach. *Numerical Linear Algebra with Applications* 2006; **13**(5):399–417.
35. Jain AK. Partial-differential equations and finite-difference methods in image-processing, part 1: image representation. *Journal of Optimization Theory and Applications* 1977; **23**(1):65–91.
36. Karras DA, Mertzios GB. New PDE-based methods for image enhancement using SOM and bayesian inference in various discretization schemes. *Measurement Science Technology* 2009; **20**(10):8.
37. Pesenson M, Roby W, McCollum B. Multiscale astronomical image processing based on nonlinear partial differential equations. *Astrophysical Journal* 2008; **683**(1):566–576.
38. Shih Y, Rei C, Wang H. A novel PDE based image restoration: convection–diffusion equation for image denoising. *Journal of Computational and Applied Mathematics* 2009; **231**(2):771–779.
39. Wu JY, Ruan QQ, An GY. Exemplar-based image completion model employing PDE corrections. *Informatica* 2010; **21**(2):259–276.
40. Chen Z, Baker NA, Wei GW. Differential geometry based solvation models I: Eulerian formulation. *Journal of Computational Physics* 2010; **229**:8231–8258.
41. Chen Z, Baker NA, Wei GW. Differential geometry based solvation models II: Lagrangian formulation. *Journal of Mathematical Biololgy* accepted, 2010.
42. Wei GW. Differential geometry based multiscale models. *Bulletin of Mathematical Biology* 2010; **27**:1562–1622.
43. Caselles V, Kimmel R, Sapiro G. Geodesic active contours. *International Journal of Computer Vision* 1997; **22**(1):61–79.
44. Chan TF, Vese LA. Active contours without edges. *IEEE Transactions on Image Processing* 2001; **10**(2):266–277.
45. Yezzi A *et al.* A fully global approach to image segmentation via coupled curve evolution equations. *Journal of Visual Communication and Image Representation* 2002; **13**(1-2):195–216.
46. Dugatkin D, Zhou HM, Chan TF, Effros M. Lagrangian optimization of a group testing for ENO wavelets algorithm. In *Proceedings to the 2002 Conference on Information Sciences and Systems, Princeton University, New Jersey*, 2002; 20–22.
47. Chan TF, Kang SH, Shen J. Euler's elastica and curvature-based inpainting. *SIAM Journal on Applied Mathematics* 2002:564–592.
48. Chambolle A, Lions PL. Image recovery via total variation minimization and related problems. *Numerische Mathematik* 1997; **76**(2):167–188.
49. Bates PW, Chen Z, Sun YH, Wei GW, Zhao S. Geometric and potential driving formation and evolution of biomolecular surfaces. *Journal of Mathematical Biology* 2009; **59**(2):193–231.
50. Greer JB, Bertozzi AL. H-1 solutions of a class of fourth order nonlinear equations for image processing. *Discrete and Continuous Dynamical Systems* 2004; **10**(1-2):349–366.

Copyright © 2011 John Wiley & Sons, Ltd.

DOI: 10.1002/cnm

51. Greer JB, Bertozzi AL. Traveling wave solutions of fourth order PDEs for image processing. *SIAM Journal on Mathematical Analysis* 2004; **36**(1):38–68.
52. Lysaker M, Lundervold A, Tai XC. Noise removal using fourth-order partial differential equation with application to medical magnetic resonance images in space and time. *IEEE Transactions on Image Processing* 2003; **12**(12):1579–1590.
53. Tasdizen T, Whitaker R, Burchard P, Osher S. Geometric surface processing via normal maps. *Acm Transactions on Graphics* 2003; **22**(4):1012–1033.
54. You YL, Kaveh M. Fourth-order partial differential equations for noise removal. *IEEE Transactions on Image Processing* 2002; **9**(10):1723–1730.
55. Bertozzi AL, Greer JB. Low-curvature image simplifiers: global regularity of smooth solutions and laplacian limiting schemes. *Communications on Pure and Applied Mathematics* 2004; **57**(6):764–790.
56. Xu M, Zhou SL. Existence and uniqueness of weak solutions for a fourth-order nonlinear parabolic equation. *Journal of Mathematical Analysis and Applications* 2007; **325**(1):636–654.
57. Jin ZM, Yang XP. Strong solutions for the generalized Perona–Malik equation for image restoration. *Nonlinear Analysis-theory Methods and Applications* 2010; **73**(4):1077–1084.
58. Witelski TP, Bowen M. ADI schemes for higher-order nonlinear diffusion equations. *Applied Numerical Mathematics* 2003; **45**(2-3):331–351.
59. Wang Y, Wei G, Yang S. Mode decomposition evolution equations. *submitted*, 2010.
60. Lin L, Wang Y, Zhou H. Iterative filtering as an alternative algorithm for empirical mode decomposition. *Advances in Adaptive Data Analysis* 2009; **1**(4):543–560.
61. Wang Y, Wei G, Yang S. Iterative filtering decomposition based on local spectral evolution kernel. *Journal of Scientific Computing* accepted, 2011.
62. Gilboa G, Sochen N, Zeevi YY. Forward-and-backward diffusion processes for adaptive image enhancement and denoising. *IEEE Transactions on Image Processing* 2002; **11**(7):689–703.
63. Gilboa G, Sochen N, Zeevi YY. Image sharpening by flows based on triple well potentials. *Journal of Mathematical Imaging and Vision* 2004; **20**(1-2):121–131.
64. Didas S, Weickert J, Burgeth B. Properties of higher order nonlinear diffusion filtering. *Journal of Mathematical Imaging and Vision* 2009; **35**(3):208–226.
65. Hou ZJ, Wei GW. A new approach to edge detection. *Pattern Recognition* 2002; **35**(7):1559–1570.
66. Chen D, Wei GW. Modeling and simulation of nano-electronic devices. *Journal of Computational Physics* 2010; **229**:4431–4460.
67. Yang S, Coe JD, Kaduk B, Martínez TJ. An optimal spawning algorithm for adaptive basis set expansion in nonadiabatic dynamics. *Journal of Chemical Physics* 2009; **130**:134113.
68. Grinvald A, Lieke E, Frostig RD, Gilbert CD, Wiesel TN. Functional architecture of cortex revealed by optical imaging of intrinsic signals. *Nature* 1986; **324**:361–364.
69. Izhaky D, Nelson DA, Burgansky-Eliash Z, Grinvald A. Functional imaging using the retinal function imager: direct imaging of blood velocity, achieving fluorescein angiography-like images without any contrast agent, qualitative oximetry, and functional metabolic signals. *Japanese Journal of Ophthalmology* 2009; **53**(4):345–351.

Copyright © 2011 John Wiley & Sons, Ltd.

DOI: 10.1002/cnm